Draft version April 18, 2024
Typeset using LaTeX **twocolumn** style in AASTeX631

Identifying coronal sources of L1 solar wind disturbances using the Fisk heliospheric magnetic field and potential field extrapolations during three solar minima

P. J. Steyn [1] D. Johnson [2,3] G. J. J. Botha [2] and S. Régnier [2]

[1] *Centre for Space Research, North-West University, Potchefstroom, South Africa, 2522*
[2] *Department of Mathematics, Physics and Electrical Engineering, Northumbria University, Newcastle upon Tyne, NE1 8ST, United Kingdom*
[3] *School of Mathematics and Statistics, University of St Andrews, St Andrews, Fife, KY16 9SS, United Kingdom*

(Received November 15, 2023; Revised February 24, 2024; Accepted March 11, 2024)

ABSTRACT

The solar minima between solar cycles 22-23, 23-24 and 24-25 are the best observed minima on record. In situ solar wind and interplanetary magnetic field measurements by the WIND and ACE spacecraft at L1 with one-hour cadence are explored using wavelet analyses for the most quiescent year during each minimum. Times of local peaks in periodicities are identified in the solar wind velocity, magnetic field components, and proton number densities. The measured radial velocities at these times are used to trace magnetic field lines to the photosphere using two models. The first is the Fisk heliospheric magnetic field that traces field lines from L1 to the photosphere. They connect exclusively to solar poles and in 88% instances to locations of polar coronal holes. The second model uses the Parker spiral to trace from L1 to the solar source surface and potential field extrapolations from the source surface to the photosphere. These field lines terminate at equatorial and mid-latitude coordinates of which some are located close to coronal holes. This study connects for the first time coronal hole signatures in the ecliptic plane at L1 with polar coronal holes using the Fisk field. It shows how sources from both the solar equator and poles influence the solar wind at L1 and how the two models compliment each other to identify these sources.

Keywords: Solar coronal holes(1484) — Solar magnetic fields(1503) — Lagrangian points(897) — Solar wind(1534) — potential field extrapolation

1. INTRODUCTION

Epochs of solar minima present unique opportunities to study the properties of the solar wind. While direct in situ measurements of the solar wind were first made in the early 1960s (Neugebauer & Snyder 1962), continuous, high-resolution data were not available until the mid 1990s. As a result, the last three solar minima, between cycles 22-23 (1996/1997), 23-24 (2008/2009), and 24-25 (2019/2020) are the best observed minima on record (Jian et al. 2011; Carrasco & Vaquero 2021; Riley et al. 2022). The aim of this study is to investigate the observed solar wind disturbances at the L1 Lagrangian point upstream of Earth during the previous three solar minima and their connection to solar coronal holes (CHs). Previous studies, such as Luhmann et al. (2022), report that low to mid-latitude CHs dominate upstream plasma measurements and has an impact on space weather.

It is known that the 27-day synodic solar equatorial rotation period is observed in the solar wind (Mursula & Zieger 1996). Due to the differential rotation of the photosphere, which in turn influences the corona, periodicities between 25 and 30 days are observed during low solar activity (Luhmann et al. 2022).

This paper uses the observed periodicities in the radial, tangential, and normal components of both the solar wind velocity and the interplanetary magnetic field (IMF) as a proxy to trace field lines between the photosphere and L1. Proton number densities are also investigated. The photospheric origin of these components are

Corresponding author: Ruhann Steyn
Ruhann.Steyn@wnu.ac.za

of particular interest. A Fisk heliospheric magnetic field (HMF) model is assumed between L1 and the solar wind source surface (SWSS) after which the field lines are mapped to the photosphere using heliographic and heliomagnetic coordinate transformations around the tilt angle α (Fisk 1996; Zurbuchen et al. 1997; Fisk et al. 1999). For comparison, a standard Parker HMF (Parker 1958) configuration is assumed between L1 and the SWSS after which the field lines are mapped to the photosphere incorporating potential field source surface (PFSS) extrapolations. The assumption of a background Parker field in the ecliptic plane has been used in numerous studies (Li et al. 2016; Strauss et al. 2017; Zhao et al. 2017). Posner et al. (2001) used the Fisk HMF to study magnetic reconnection processes at the boundaries of CHs by investigating solar wind composition measurements from the Ulysses spacecraft at large radial distances ($\sim$ 4 AU near the streamer belt). The scope of this paper, however, is constrained to the ecliptic plane and L1.

Due to ease of use, many studies use PFSS from the solar surface to the SWSS and model the Parker HMF beyond the SWSS (Owens & Forsyth 2013; Balogh & Erdõs 2013). Alternative methods tracing magnetic field lines from the solar surface to the SWSS exist, such as non-linear force free fields and steady-state magnetohydrodynamics (Parenti et al. 2021), magnetofrictional relaxation (Yeates et al. 2018), force-free electrodynamics (Contopoulos 2013) and the solar-interplanetary space-time conservation element and solution element magnetohydrodynamic (SIP-CESE MHD) model of Yang et al. (2012). Alternative methods to trace the HMF from the solar surface into the heliosphere are relaxation of magnetic field lines (Gilbert et al. 2007), steady-state magnetohydrodynamic models (Garraffo et al. 2013) and the Fisk model (Fisk 1996; Zurbuchen et al. 1997). Zhao et al. (2017) point out that in spite of its approximations, the PFSS and Parker combination is useful to identify solar wind source regions from solar wind measurements on the ecliptic plane. This study will compare its results with the standard non-modified Fisk HMF between L1 and the photosphere.

The solar wind can be characterised by proton speed and heavy ion charge states, such as O^{7+}/O^{6+} and O^{6+}/O^{5+} oxygen ratios (Zhao et al. 2017). The solar wind speed varies as it moves towards L1 (Jain et al. 2024). In addition, the solar wind originating from equatorial CHs contains fast as well as slow components (Wang et al. 2009; Stakhiv et al. 2015) and the various plasma populations interact with one another (Stansby et al. 2019). In this study, as will be shown later, a constant solar wind speed is assumed. The constraints of assuming a constant speed are mitigated by investigating measurements over a time interval at L1, rather than using a velocity at one time instant. The obtained results are then corroborated by taking oxygen ratios over the same time interval.

The data retrieval and processing is explained in Section 2, an introduction to the two models is described in Section 3, the wavelet analyses of the three solar minima are presented in Section 4, the Carrington maps are shown in Section 5, and the concluding remarks are made in Section 6.

2. DATA

2.1. *Solar wind and interplanetary magnetic field*

One-hour cadence solar wind velocity component measurements and proton number density measurements for the three observed solar minima are from the Wind/SWE data sets (Ogilvie et al. 1995; Wilson et al. 2021). The IMF measurements are from the Wind/MFI instrument (Lepping et al. 1995) for the 1996 solar minimum and from the ACE Magnetic Field Experiment data sets (Smith et al. 1998) for the remaining solar minima. Time periods of one year, based on the lowest monthly smoothed sunspot number (SILSO World Data Center 1996-2020), are used for each solar minimum epoch investigated in this study. The solar wind velocity data are converted from the GSE (geocentric solar magnetospheric) system of coordinates to the RTN (radial, tangential, normal) system of coordinates as follows,

$$V_r = -V_x, \quad V_t = -V_y, \quad V_n = V_z, \tag{1}$$

where V_r, V_t, and V_n are the radial, tangential and normal solar wind velocity components respectively. The same conversions are followed for the IMF data. Known interplanetary coronal mass ejections (ICMEs) are removed from the solar wind and magnetic field data sets according to the ICME database of Richardson & Cane (2010). We replace the ICME data with Gaussian white noise with a mean and standard deviation computed from the data before and after the ICME. This successfully removes their signal from the wavelet analyses.

2.2. *Carrington Maps*

For the 1996 solar minimum, a set of Carrington maps is available from the SOHO/EIT Synoptic Map Database (Benevolenskaya et al. 2001; Benevolenskaya 2001), which provides maps for Carrington rotations (CRs) 1911 to 2055. These Carrington maps are restricted to $\pm 83°$ due to Earth's changing vantage point (Hamada et al. 2018). Carrington maps for the 2008/2009 and 2019/2020 solar minima are assembled from full-disk solar images obtained from the European

Space Agency's SOHO Science Archive database (ESA 2023) using the 195Å wavelength. The Carrington maps are assembled following the methods of Thompson et al. (1997) and Thompson (2006) where slices of 13.3° longitude (corresponding to one day's CR length scale) are extracted centred on the central meridian. The tilt angle α for each CR is from Hoeksema (1995)[1].

2.3. *Photospheric magnetic field*

This study uses the PFSS packages[2] included in SolarSoft (Freeland & Handy 1998; Schrijver & De Rosa 2003). The magnetograms used in the PFSS model to determine the configuration of the photospheric magnetic field are from SOHO/MDI (Domingo et al. 1995; Scherrer et al. 1995) for the solar minima of 1996/1997 and 2008/2009. Magnetograms from the HMI instrument (Scherrer et al. 2012) onboard SDO (Pesnell et al. 2012) are used for the 2019/2020 solar minimum. The magnetograms used by this PFSS model is not controlled by the user.

2.4. *Coronal holes*

The locations and polarity of CHs are confirmed by the daily National Oceanic and Atmospheric Administration (NOAA) solar synoptic analysis charts (NOAA 1996-2020). In addition, the heavy ion charge state ratio (O^{7+}/O^{6+}) obtained from ACE observations is used to confirm the locations of coronal holes.

3. MAGNETIC FIELD MODELS

3.1. *Fisk heliospheric magnetic field model*

The tracing of Fisk magnetic field lines expanding from polar coronal holes (PCHs) are discussed in this section. Fisk (1996) introduced a novel HMF model in an effort to explain the recurrent energetic particle events observed at high latitudes by the Ulysses spacecraft (Simpson et al. 1995). Figure 1 shows the geometry of the model proposed by Fisk (1996). The rotational axis $\boldsymbol{\Omega}$ is separated from the magnetic axis $\mathbf{M}$ by a tilt angle α. The $\hat{\mathbf{p}}$-axis is defined by the magnetic field line originating from the solar pole where no differential rotation is assumed and is separated from the rotational axis by an angle β. Fisk-type field lines are assumed to originate from rigidly-rotating PCHs (the source of the fast solar wind) and to expand from the photosphere to the source surface symmetrically about the magnetic axis. The differential rotation of the field line footpoints on the photosphere and the super-radial expansion of field lines to the source surface cause the Fisk model to display large excursions in heliographic latitude. This unique characteristic makes this HMF model a good candidate to trace field lines from L1 back to their coronal, and subsequently, their photospheric origin. The expansion of the field lines form footpoint trajectories on the source surface symmetric about the $\hat{\mathbf{p}}$-axis. Zurbuchen et al. (1997) report the expression of the field to be

$$\mathbf{B} = B_0 \left(\frac{r_o}{r}\right)^2 \left[\hat{\mathbf{e}}_r - \frac{r\omega}{V}\hat{\mathbf{e}}_\theta - \frac{(\Omega-\omega)r\sin\theta}{V}\hat{\mathbf{e}}_\phi\right], \quad (2)$$

where r represents the radial distance away from the sun, B_0 is the field strength at r_0, V is the solar wind speed, ω the differential rotation rate of the photosphere (typically assumed to be a constant fraction of the solar equatorial rotation rate Ω, i.e., $\Omega/4$), and θ the heliographic co-latitude from which the field line expands. Note that for $\theta = 90°$ (the solar equator) and $\omega = 0$ rads/sec (no differential rotation) equation (2) reduces to the standard Parker HMF expression (Parker 1958). Since each field line trace is unique, field lines can be traced from the source surface to the photosphere using this method. Steyn & Burger (2020) report this tracing in three distinct processes. Firstly, a transformation about the tilt angle α from heliographic to heliomagnetic coordinates on the source surface is performed (equations (3) and (4)). Next, the tracing from the source surface to the photosphere in both latitude and longitude is done based on the Divergence Theorem (equations (5) and (6)), and finally a transformation about the tilt angle from heliomagnetic to heliographic coordinates are performed (equations (7) and (8)). This process is described by the following expressions

$$\theta^{ss}_{hm} = \cos^{-1}(\cos\theta^{ss}_{hg}\cos\alpha + \sin\theta^{ss}_{hg}\sin\alpha\cos\phi^{ss}_{hg}), \quad (3)$$

$$\phi^{ss}_{hm} = \cos^{-1}\left(\frac{\sin\theta^{ss}_{hg}\cos\phi^{ss}_{hg}\cos\alpha - \cos\theta^{ss}_{hg}\sin\alpha}{\sin\theta^{ss}_{hm}}\right), \quad (4)$$

$$\theta^{ph}_{hm} = \sin^{-1}\left(\sqrt{\frac{(1-\cos\theta^{ss}_{hm})\sin^2\theta^{ph}_{mm}}{(1-\cos\theta^{ss}_{mm})}}\right), \quad (5)$$

$$\phi^{ph}_{hm} = \phi^{ss}_{hm}, \quad (6)$$

$$\theta^{ph}_{hg} = \cos^{-1}(\cos\theta^{ph}_{hm}\cos\alpha - \sin\theta^{ph}_{hm}\cos\phi^{ph}_{hm}\sin\alpha), \quad (7)$$

$$\phi^{ph}_{hg} = \cos^{-1}\left(\frac{\cos\theta^{ph}_{hm}\sin\alpha + \sin\theta^{ph}_{hm}\cos\phi^{ph}_{hm}\cos\alpha}{\sin\theta^{ph}_{hg}}\right), \quad (8)$$

where the subscripts hg and hm refers to heliographic and heliomagnetic coordinates respectively, and the superscripts ss and ph refers to the source surface and photosphere respectively, and where $\sin\theta^{ss}_{hm} \neq 0$, $\cos\theta^{ss}_{mm} \neq 1$, and $\sin\theta^{ph}_{hg} \neq 0$. The boundaries of the PCHs in heliomagnetic coordinates on the photosphere and source

[1] http://wso.stanford.edu/Tilts.html

[2] https://www.lmsal.com/~derosa/pfsspack

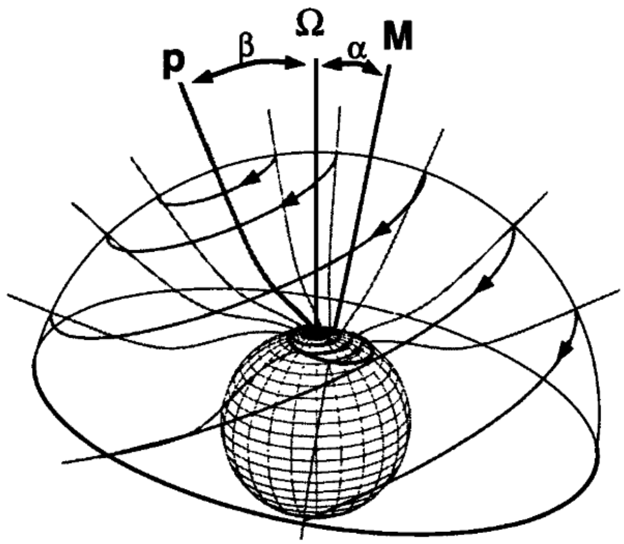

Figure 1. An illustration of the expansion of magnetic field lines from the photosphere to the SWSS from rigidly rotating PCHs according to the Fisk HMF model. The direction of the footpoint trajectories are shown on the source surface. The rotation axis $\mathbf{\Omega}$, the magnetic axis $\mathbf{M}$, the $\hat{\mathbf{p}}$ axis, the tilt angle α, and the Fisk-angle β are shown. Figure adapted from Zurbuchen et al. (1997).

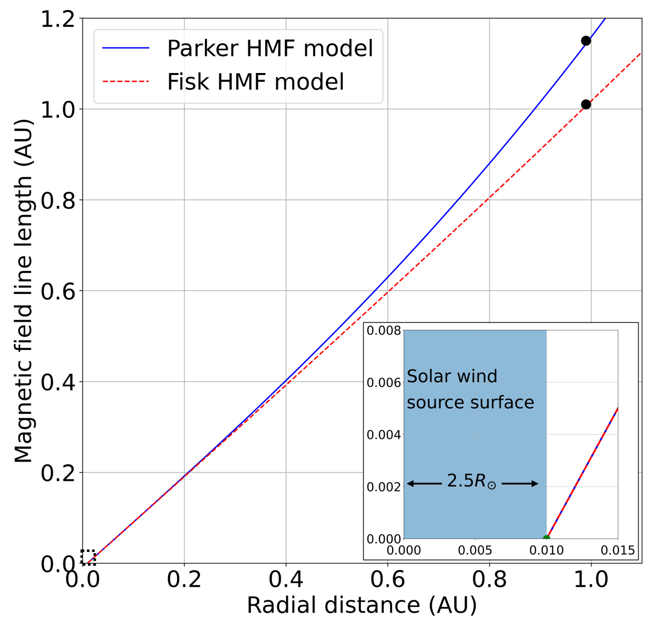

Figure 2. Magnetic field line lengths of the Parker (solid blue) and Fisk (dashed red) HMF models between the SWSS and L1. The black dots refers to the L1 position at $r = 0.99$ AU. The insert graph is of the square at the origin of the main graph showing the starting point of the magnetic field lines at the SWSS boundary located at $r = 2.5R_\odot = 0.01$ AU.

surface are represented by θ^{ph}_{mm} and θ^{ss}_{mm} and their values are chosen to be 24° and 70° respectively, in accordance to the example shown in Fisk (1996).

This study assumes that the measured radial solar wind velocity (V_r) remains constant between L1 and the SWSS during the time of tracing a field line. The length of a magnetic field line from L1 at $r = 0.99$ AU to the SWSS at $r_0 = 2.5R_\odot = 0.01$ AU is determined by $S = \int_{r_0}^{r} |d\ell|$ where $|d\ell|^2 = dr^2 + r^2 d\theta^2 + r^2 \sin^2\theta d\phi^2$ in spherical coordinates. V_r measured at the time of the local maximum in the period at L1 is used together with S to calculate the difference between Sun-time and L1-time. The small, but nonetheless non-zero, difference between the Parker (1.14 AU) and Fisk (1.01 AU) field line lengths due to different $d\ell$ expressions for the two HMF configurations are shown in Figure 2 for a constant solar wind velocity of 400 km/s.

3.2. *Potential field source surface model*

The PFSS extrapolation method was developed and refined by Schatten et al. (1969), Altschuler & Newkirk (1969), Hoeksema (1984), and Wang & Sheeley (1992). In this study, the upper boundary condition of the PFSS model is located at the SWSS, assumed to be spherical and a radial distance $2.5R_\odot$ from the photosphere. The lower boundary condition is the photospheric magnetic field generated from full-disk magnetograms. The magnetograms used in this study are from two different instruments as mentioned in Section 2.3 which influences the comparability of the PFSS results between solar minima. Previous studies, such as Luhmann et al. (2022), use magnetograms from a single instrument. Furthermore, Hofmeister et al. (2019) report a connection between long-lived (more than 40 hours) photospheric magnetic elements and the magnetic flux of CHs. Wang et al. (1996) explain that the locations of CHs can be reproduced and better understood by applying extrapolation models to measurements of the photospheric magnetic field. These authors show that the solar wind speed and solar wind flux densities can be related to the magnetic field strength of CHs. Therefore, the PFSS model is advantageous to trace field lines from the SWSS to the photosphere since it considers the prevailing configuration of the photospheric magnetic field and, in principle, convey information about the state of the coronal magnetic field. Figures 3(a) and 3(b) illustrate an example of the tracing of a continuous magnetic field line from the SWSS to the photosphere in both heliographic latitude (θ_{hg}) and longitude (ϕ_{hg}) using the PFSS model. Small latitudinal and longitudinal perturbations, such as shifting θ^{ss}_{hg} and ϕ^{ss}_{hg} by 1°, have a minimal effect on the results of θ^{ph}_{hg} and ϕ^{ph}_{hg} which implies stable results for the investigated solar minima. A standard Parker field is assumed between L1 and the SWSS when tracing a field line for the PFSS model.

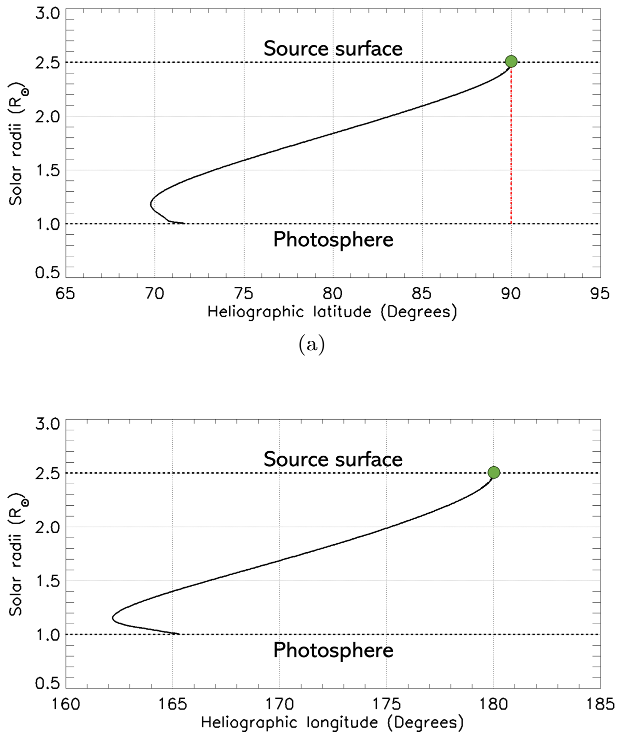

Figure 3. A magnetic field line trace from the source surface at $2.5R_\odot$ down to the photosphere at $1.0R_\odot$. The green dot represents the entry point at the SWSS. (a) shows the trace from $\theta_{hg}^{ss} = 90°$ to $\theta_{hg}^{ph} = 71.6°$. The equator is indicated by the vertical red dot-dashed line. (b) shows the same trace in heliographic longitude from $\phi_{hg}^{ss} = 180°$ to $\phi_{hg}^{ph} = 165.6°$.

The length of the Parker magnetic field line is shown in Figure 2 and the difference between sun-time and L1-time is calculated in the same way as in Section 3.1, again assuming that the measured V_r remains constant between L1 and the SWSS.

4. SOLAR WIND AND IMF PROPERTIES AT L1

4.1. *1996/1997 solar minimum*

The following section focuses on the solar minimum period between 1 February 1996 to 31 January 1997 (365 days). Figure 4 shows the wavelet results for the radial solar wind velocity V_r (Figure 4(a)), the proton number density n_i (Figure 4(b)), the normal B_n (Figure 4(c)), and tangential B_t (Figure 4(d)) magnetic field components. Table 1 summarises the results from the wavelet analysis, including the date at which the maximum period was observed at L1, the maximum period in days (ranging between 26.2 and 31.2 days), and the corresponding Carrington rotation (CR) during which the maximum occurred. The pairs of wavelets with maxima at approximately the same date include V_r and n_i, V_r and B_n, and n_i and B_t as seen in Figure 4. The first maxima observed in V_r and n_i on 5 April 1996 (day 64) and 18 April 1996 (day 77), respectively, are part of CRs 1907 and 1908. Although these Carrington maps are not available (see Section 2.2), the maxima in V_r and n_i are included in Figure 4 and Table 1 to illustrate the observed periodicity. The maximum observed in B_n on 3 October 1996 (day 245 of Figure 4(c)) during CR1914 corresponds to the second maximum observed in V_r on the same day (Figure 4(a)). The maximum observed in n_i on 4 December 1996 (day 307 of Figure 4(b)) is coupled together with the maximum observed on 21 November 1996 (day 294 of Figure 4(d)) in B_t. In each group of wavelets for all three solar minima studied in this paper, the dates of the maxima observed in several of the solar wind and magnetic field components are used to trace field lines between L1 and the SWSS. However, some components are not traced between L1 and the SWSS since they share a maximum at approximately the same time as another component and rather used as a confirmation of the signal observed. For example, V_r and B_n in Table 1 have their maxima on the same date (3 October 1996) and only V_r is traced to the SWSS. The double dash in the last column of Table 1 indicates that this field line is not traced. The convention is followed throughout the study.

Table 1. 1996/1997 solar minimum with details of maxima in periodicity power at L1 as shown in Figure 4.

	Date of max	Period (Days)	CR	Figures
V_r	5 Apr. 1996	28.5	1907	4(a) ; −−
	3 Oct. 1996	31.2	1914	4(a) ; 8(a)
n_i	18 Apr. 1996	26.2	1908	4(b) ; −−
	4 Dec. 1996	26.2	1916-1917	4(b) ; 8(c)
B_n	3 Oct. 1996	26.2	1914	4(c) ; −−
B_t	21 Nov. 1996	28.5	1915-1916	4(d) ; 8(b),8(c)

4.2. *2008/2009 solar minimum*

The following section focuses on the solar minimum period between 6 July 2008 and 6 July 2009 (365 days) and describes the same process followed in Section 4.1. Figure 5 shows six wavelets including V_r (Figure 5(a)), V_t (Figure 5(b)), V_n (Figure 5(c)), n_i (Figure 5(d)), B_r (Figure 5(e)), and B_t (Figure 5(f)). Table 2 summarises the details of this solar minimum.

The wavelets from Figure 5 that share periodicities at approximately the same time include V_r and n_i on 17 September 2008 (day 70), the trio of measurements V_t on

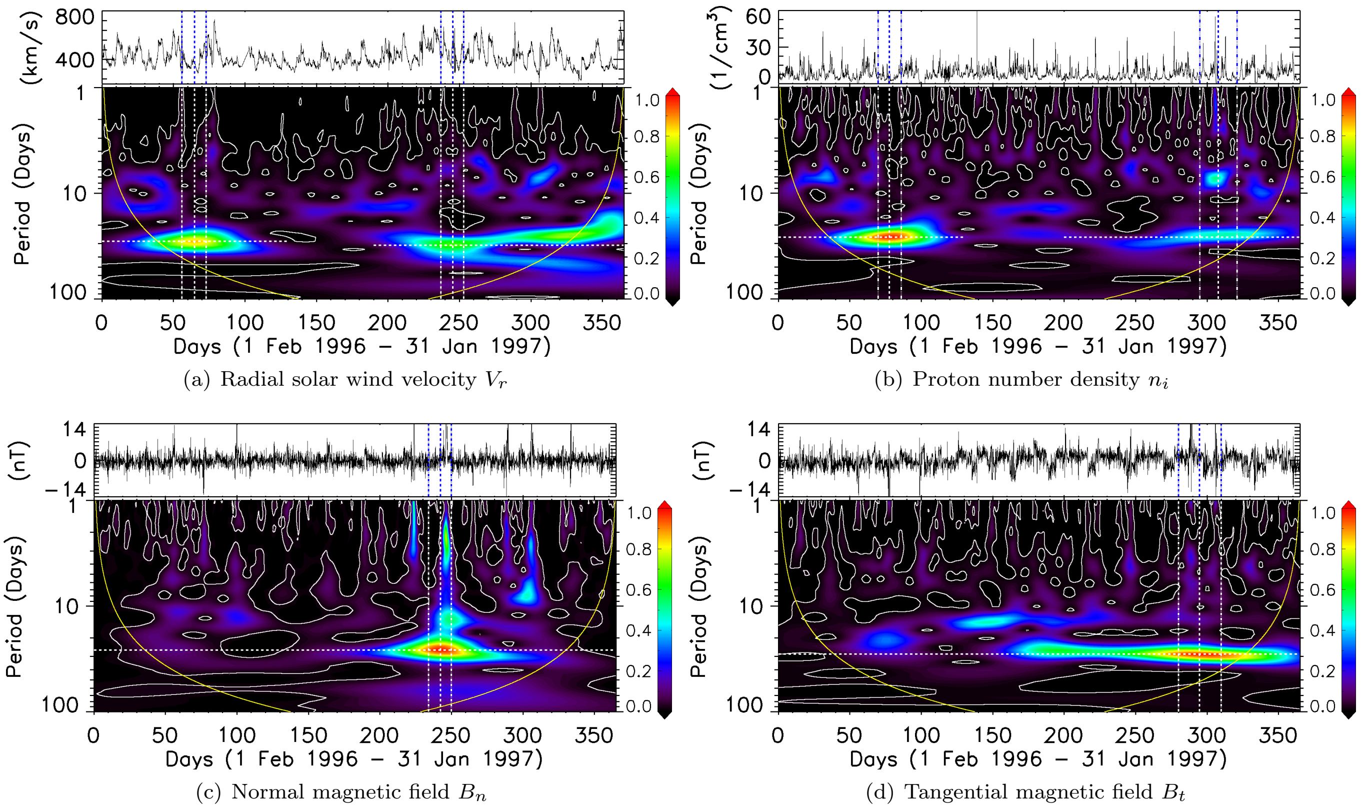

(a) Radial solar wind velocity V_r

(b) Proton number density n_i

(c) Normal magnetic field B_n

(d) Tangential magnetic field B_t

Figure 4. Wavelets indicating the signals and periodicities of the (a) radial solar wind velocity, the (b) proton number density, the (d) normal and (e) tangential magnetic field components between 1 February 1996 and 31 January 1997 during the 1996/1997 solar minimum epoch. The panel above each wavelet shows the input data. The three vertical white dashed lines show the time of local maximum power (central line) of the dominant periodicity with the two side lines showing the times of a 5% reduction from peak power. The same are shown in blue in the input data panel. The horizontal white dashed lines indicate the dominant periodicity. The normalised power of each periodicity is identified by the colour scale, while the cone of influence is indicated in yellow. The white contour shows the 99.5% confidence level.

13 October 2008 (day 99), B_r on 21 October 2008 (day 107) and B_t on 28 October 2008 (day 114), and finally V_n on 21 March 2008 (day 258) and B_r on 18 April 2008 (day 286). Note that the first maximum of B_r (day 43 on 17 August 2008 of Figure 5(e)) is included in Table 2, but is not used in further analyses since the 5% decrease in intensity to the left of the maximum is inside the cone of influence (COI). There is also no confirmation of this signal since the maximum intensity of the periodicity identified at approximately the same time in B_t (Figure 5(f)) is also inside the COI. V_n (Figure 5(c)) and the third maximum of B_r (Figure 5(e)) have a 28-day gap between their respective local maxima shown in Table 2. Due to the long duration of the observed periodicity in both V_n and B_r, they might share a common physical process giving rise to the signal at L1.

V_r shows a period of 26.2 days on 17 September 2008 (day 73 of Figure 5(a)). V_t shows a period of 26.2 days approximately a month later on 13 October 2008 (day 99 of Figure 5(b)). Additionally, Figure 5(b) also shows short term ($\sim$ 2.5 days), short periodicity ($\sim$ 1.5 days) vertical structures with high-power signals. The top panel confirms that these strong, short-term periodicities are caused by peaks in V_t. Although all known ICMEs were removed from the data sets, it is possible for different transient events to be observed in the data. These events were not removed for the sake of consistency and transparency. V_n shows a period of 28.5 days on 21 March 2009 (day 258 of Figure 5(c)). n_i follows the behaviour of V_r closely with a period of 26.2 days also occurring on 17 September 2008 (day 73). Peaks in n_i are accompanied by strong, short-term power signals. Next, Figures 5(e) and 5(f) show B_r and B_t results respectively. Both figures show long duration power signals at periods of 28.5 days (B_r) and 26.2 days (B_t). Three local maxima are observed in B_r and are indicated on Figure 5(e). Table 2 shows the maxima of B_r occurring on 17 August 2008 (day 42), 21 October 2008 (day 107), and 18 April 2009 (day 286), and the maximum of B_t occurring on 28 October 2008 (day 115).Note that the periodicities are only identified in order to select the date and time the field lines are traced back

Table 2. 2008/2009 solar minimum with details of maxima in periodicity power at L1 as shown in Figure 5.

	Date of max	Period (Days)	CR	Figures
V_r	17 Sept. 2008	26.2	2074	5(a) ; 9(a)
V_t	13 Oct. 2008	26.2	2075	5(b) ; 9(b)
V_n	21 March 2009	28.5	2081	5(c) ; 9(c),9(d)
n_i	17 Sept. 2008	26.2	2074	5(d) ; −−
B_r	17 Aug. 2008	26.2	2073	5(e) ; −−
	21 Oct. 2008	28.5	2075	5(e) ; −−
	18 Apr. 2009	28.5	2082	5(e) ; 9(d)
B_t	28 Oct. 2008	26.2	2075	5(f) ; 9(b)

Table 3. 2019/2020 solar minimum with details of maxima in periodicity power at L1 as shown in Figure 6.

	Date of max	Period (Days)	CR	Figures
V_r	22 Aug. 2019	26.2	2220-2221	6(a) ; 10(b)
	6 Jan. 2020	24.0	2225-2226	6(a) ; −−
V_n	29 Jul. 2019	31.17	2220	6(b) ; −−
	4 Jan. 2020	26.2	2225	6(b) ; −−
n_i	25 Aug. 2019	28.5	2220-2221	6(c) ; −−
	9 Jan. 2020	24.0	2225-2226	6(c) ; −−
B_r	6 Aug. 2019	28.5	2219-2220	6(d) ; 10(a),10(b)
	14 Dec. 2019	26.2	2224-2225	6(d) ; −−
B_t	30 Jul. 2019	28.5	2219-2220	6(e) ; −−
	20 Dec. 2019	26.2	2224-2225	6(e) ; 10(c)
B_n	10 Jan. 2020	24.0	2225-2226	6(f) ; 10(c) 10(d)

from L1 to the SWSS and then mapped to the photosphere. It is well-known that the harmonic structure of the solar synoptic rotation has an imprint in the solar wind (Prabhakaran Nayar et al. 2002; Singh & Badruddin 2019; Tsichla et al. 2019). In this study we focus on the fundamental frequency only and use its maximum power to determine the time of maximum disturbance at L1.

4.3. *2019/2020 solar minimum*

The same process as in Sections 4.1 and 4.2 is now followed for the 2019/2020 solar minimum defined between 1 June 2019 and 31 May 2020 (365 days). Figure 6 shows the wavelet results for V_r (Figure 6(a)), V_n (Figure 6(b)), n_i (Figure 6(c)), B_r (Figure 6(d)), B_t (Figure 6(e)) and B_n (Figure 6(f)). Table 3 summarises the details of this solar minimum epoch. The first pair of wavelets with maxima at approximately the same date during this solar minimum is V_r on 22 August 2019 (day 82) and n_i on 25 Augusts 2019 (day 85). The next trio of measurements grouped together are V_n on 29 July 2019 (day 58), B_r on 6 August 2019 (day 66) and B_t on 31 July 2019 (day 60). The third pair is B_r on 14 December 2019 (day 196) and B_t on 20 December 2019 (day 202). Lastly, the following four measurements show a local maximum at approximately the same date: V_r on 6 January 2020 (day 219), V_n on 4 January 2020 (day 217), n_i on 9 January 2020 (day 222) and B_t on 20 December 2020 (day 202).

5. MAGNETIC CONNECTION FROM L1 TO THE PHOTOSPHERE

The maximum periodicities observed at L1 in Figures 4, 5, and 6 are now traced to their solar origins and shown on Carrington maps. The tracing is done along Fisk and Parker magnetic field lines connecting L1 with the SWSS (Figure 2). Next, the Fisk field lines are mapped to the photosphere using the transformations from Section 3.1 while the Parker field lines are mapped to the photosphere using the PFSS model from Section 3.2. Figure 7 shows one-week moving averages (red) of B_r for the 1996/1997 (top), 2008/2009 (middle), and 2019/2020 (bottom) solar minima. A sixth-order polynomial approximation curve (black) is fitted to the moving average. The vertical dashed lines (purple) indicate the dates of the periodicities from Tables 1, 2, and 3. The intersection between the polynomial approximation and the dates of peak periodicities indicate whether B_r is positive or negative for that date. This informs whether the magnetic field line tracing is above or below the heliospheric current sheet (HCS).

During the 1996/1997 solar minimum, the polarity of the sun was positive at the northern solar pole and negative at the southern solar pole ($A > 0$ solar cycle). Therefore, a positive B_r value in the top panel of Figure 7 is indicative of a magnetic field line with its origin at the northern solar pole while a negative B_r value is indicative of a field line with its origin at the southern solar pole. The polarities of the PCHs are confirmed by the NOAA synoptic maps mentioned in Section 2.4. During the 2008/2009 solar minimum, the polarity of the sun was negative at the northern solar pole and positive at the southern solar pole ($A < 0$ solar cycle). Therefore, a positive B_r value in the middle panel of Figure 7 is indicative of a magnetic field line with its origin at the southern solar pole while a negative B_r value is indicative of a field line with its origin at the northern solar pole. The 2019/2020 solar minimum was an $A > 0$ solar cycle again and therefore the polarities are the same as explained during the 1996/1997 solar minimum.

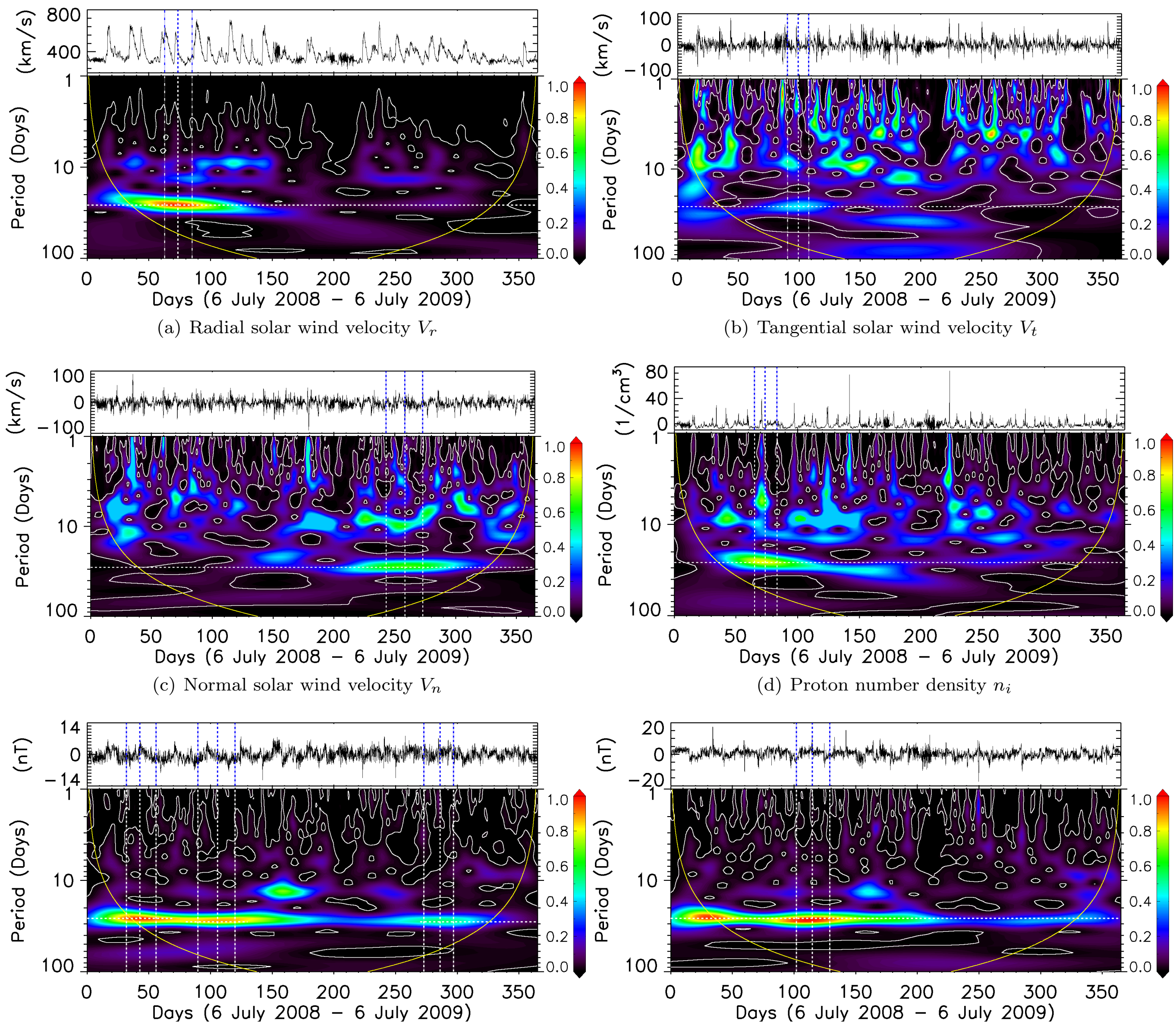

(a) Radial solar wind velocity V_r

(b) Tangential solar wind velocity V_t

(c) Normal solar wind velocity V_n

(d) Proton number density n_i

(e) Radial magnetic field B_r

(f) Tangential magnetic field B_t

Figure 5. Wavelets indicating the signals and periodicities of the (a) radial, (b) tangential and (c) normal solar wind velocities, (d) the proton number density, the (e) radial and (f) tangential magnetic field components between 6 July 2008 and 6 July 2009 during the 2008/2009 solar minimum epoch. Refer to Figure 4 for a description of the dashed lines and contours.

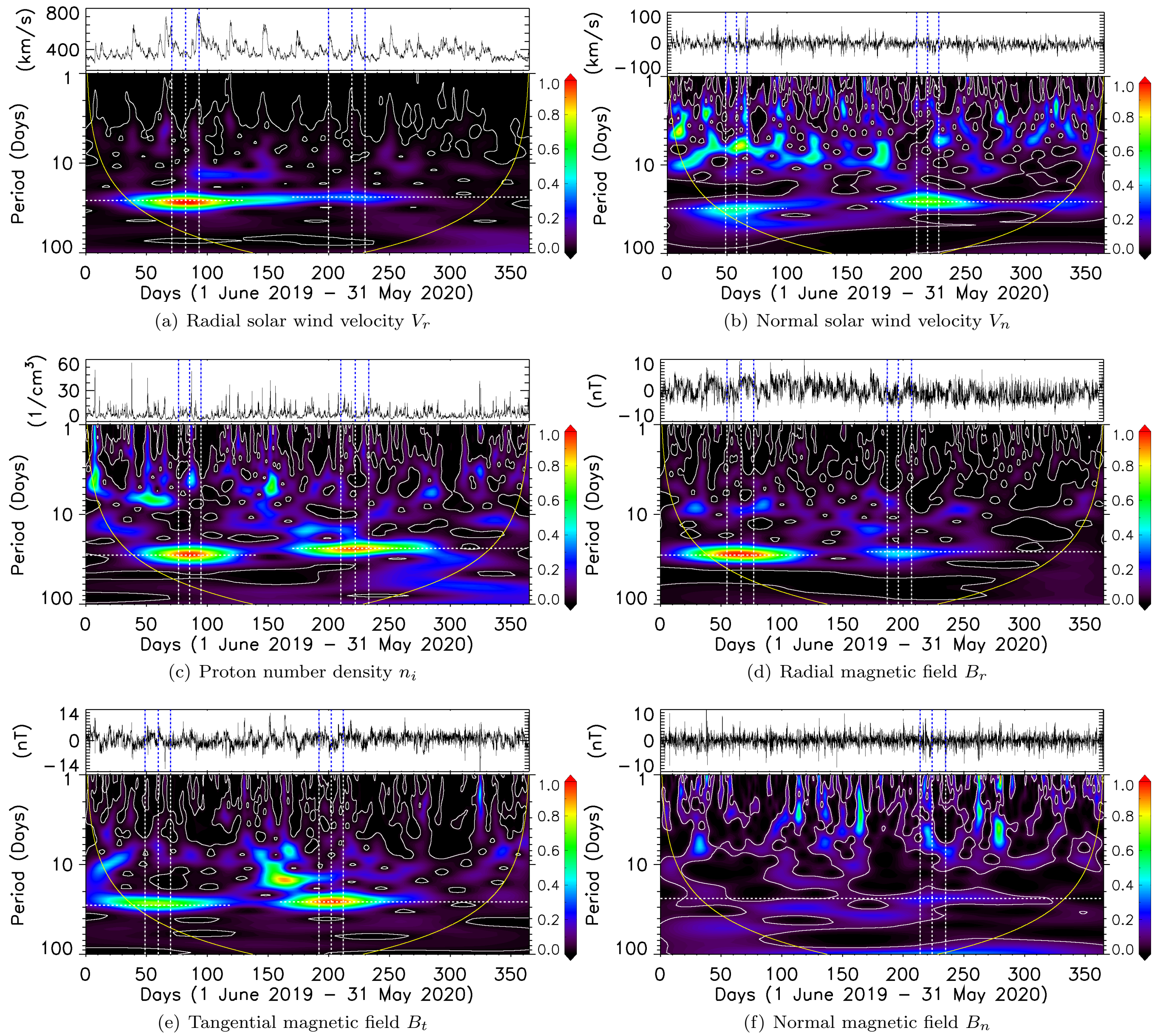

(a) Radial solar wind velocity V_r

(b) Normal solar wind velocity V_n

(c) Proton number density n_i

(d) Radial magnetic field B_r

(e) Tangential magnetic field B_t

(f) Normal magnetic field B_n

Figure 6. Wavelets indicating the signals and periodicities of the (a) radial and (b) normal solar wind velocities, (c) proton number density, the (d) radial, (e) tangential and (f) normal magnetic field components between 1 June 2019 and 31 May 2020 during the 2019/2020 solar minimum epoch. See Figure 4 for a description of the dashed lines and contours.

5.1. *1996/1997 solar minimum*

The results of the mapping of magnetic field lines from the SWSS to the photosphere for the 1996/1997 solar minimum of both the Fisk and PFSS models are shown in Figure 8 and summarised in Table 4. Three (V_r, n_i, and B_t in Table 4) of the six maxima from Table 1 are traced to the photosphere in Figure 8. The other maxima are not traced since their maxima occurs close to the already-traced maxima. The dates where the maximum power of the dominant periodicity occurred in Figure 4, together with the two dates corresponding to the 5% decrease from the maxima are traced back from L1 to the photosphere using the Fisk model (Section 3.1), as well as a Parker spiral and PFSS model (Section 3.2). It is assumed that all signals observed at L1 pass the SWSS equator. The blue circles of Figure 8 represent the entry points of the traced field lines at the SWSS equator ($2.5R_\odot$ above the photosphere) for both the Fisk and Parker HMFs. Figure 2 shows that the field lines lengths of the two HMF models are different and therefore, assuming a constant solar wind velocity (third column of Table 4) for both models, each HMF model

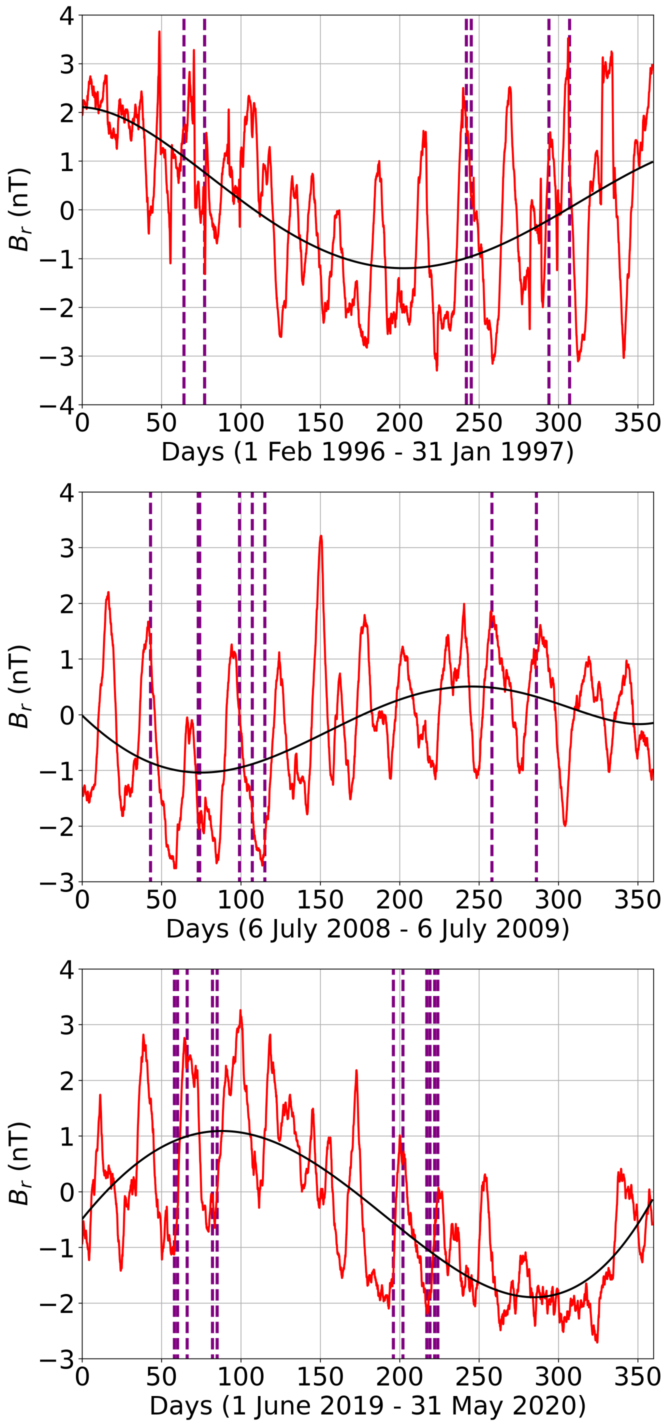

Figure 7. One-week moving averages of B_r (red) for the three investigated solar minima. A sixth-order polynomial approximation is fitted to B_r in each panel (black). The vertical dashed lines indicate the dates of maximum signals according to Figures 4, 5, and 6.

will pass the SWSS at different dates (last column of Table 4). The differences between the times and dates are too small to differentiate on the Carrington maps

Table 4. 1996/1997 solar minimum temporal field line tracing details between L1 and the SWSS for the Fisk and Parker HMFs.

	L1	V_r (km/s)	Model	SWSS
V_r	3 Oct. 1996 12:00:00	614	Parker	30 Sept. 1996 05:00:00
			Fisk	30 Sept. 1996 14:00:00
n_i	5 Dec. 1996 01:00:00	288	Parker	28 Nov. 1996 10:00:00
			Fisk	29 Nov. 1996 05:00:00
B_t	21 Nov. 1996 16:00:00	410	Parker	16 Nov. 1996 17:00:00
			Fisk	17 Nov. 1996 07:00:00

and therefore one blue circle represents the entry point of both the Fisk and Parker field lines at the SWSS in Figure 8. The blue crosses show the heliographic latitude (θ_{hg}^{ph}) to which each magnetic field line maps down from the SWSS equator to the photosphere using the PFSS model.

The red vertical lines indicate the heliographic latitudes (θ_{hg}^{ph}) to which the Fisk field lines map to on the photosphere. The length of the red vertical lines shows the uncertainty in the heliographic latitude during the mapping process brought on by the uncertainty of ϕ_{ss}^{hg} in equation (3). Cycling through $\phi_{ss}^{hg} = 0°, 90°, 180°$, and 270° provides different θ_{hg}^{ph} coordinates to which the field line maps to the photosphere. This spread of values is represented by the red vertical lines connecting the different values of θ_{hg}^{ph}. The red solid and dashed horizontal lines indicate the time duration of the signals represented by $\pm 5\%$ from the maximum power of periodicity obtained from Figure 4.

Note that the location of each blue cross symbol should not be interpreted in terms of time, since the time duration of the mapping between the SWSS and the photosphere is negligible. Rather, the location of each blue cross only represents the state of the corona when the mapping-down took place. The crosses and circles are not necessarily located on the same day on the Carrington map since there is a delay between when the mapping-down takes place and when that location is earth-facing in order to assemble the Carrington map. The same argument is true for the difference in longitude between the entry point of the Fisk field lines at the SWSS equator and the red vertical lines (indicative of ϕ_{hg}^{ph} in Equation (8)) for the results of the Fisk HMF.

The already-assembled Carrington maps shown in Figure 8 are from the SOHO/EIT Synoptic Map Database (Section 2.2). These maps are not as accurate as those presented for the next two solar minima since they are constructed with wider longitudinal strips (approximately 16°), and there are instances where even wider strips are used from the previous day to cover missing data values (Benevolenskaya et al. 2001). Therefore, the calendar dates in red on the horizontal axis of Figure 8 are only approximate dates. The darker green regions of each Carrington map show the locations of CHs.

The tracing for V_r (from Figure 4(a)) is shown in Figure 8(a). On 20 September 1996 (day 3 of CR1914), the PFSS model maps to mid-latitudes close to the vicinity of an active region (AR) (which was earth-facing on 23 September 1996). On 30 September 1996 (day 13 of CR1914) the field lines map close to the solar equator at a location with no CH activity. On 6 October 1996 (day 19 of CR1914) the field lines map to the northern mid-latitudes which is in the vicinity of a well-developed northern PCH (which was earth-facing on 9 October 1996). The results of the Fisk model mapping are shown in red. On 21 September 1996 (day 4 of CR1914) the Fisk model maps to a southern PCH. Furthermore, the Fisk field maps to two more southern PCHs on 30 September 1996 (day 13) and 7 October 1996 (day 20) of the same CR. Note that large northern PCHs are visible during CR1914, but the Fisk field do not map to these due to the orientation of the HCS shown in the top panel of Figure 7.

The blue circle in Figure 8(b) represents the equatorial SWSS entry point of both Fisk and Parker field lines traced from the maximum of B_t in Figure 4(d) on day 19 during CR1915 (1 November 1996). The corresponding blue cross in Figure 8(b) is not close to the location of visible CHs, while the red vertical line maps into a southern PCH (day 20 during CR1915 on 2 November 1996) which extends into CR1916 (Figure 8(c)). The remaining blue circles and crosses in Figure 8(c) during CR1916 are from B_t (Figure 4(d)) crossing the SWSS equator on 16 November 1996 (day 6) and 30 November 1996 (day 20) where both field lines map near the photospheric equator. The yellow symbols in Figure 8(c) during CRs 1916 and 1917 refer to the maximum observed in n_i (Figure 4(b)). The first SWSS entry of n_i is made 17 November 1996 (day 7 of CR1916), the maximum of n_i is mapped on 28 November 1996 (day 18 of CR1916), and the last field line from n_i is mapped on 12 December 1996 (day 5 of CR1917). All the PFSS results during CRs 1916 and 1917 map close to the solar equator and are not located near CH activity.

Table 5. 2008/2009 solar minimum temporal field line tracing details between L1 and the SWSS for the Fisk and Parker HMFs.

	L1	V_r (km/s)	Model	SWSS
V_r	17 Sept. 2008 15:00:00	423	Parker	12 Sept. 2008 20:00:00
			Fisk	13 Sept. 2008 09:00:00
B_t	28 Oct. 2008 20:00:00	288	Parker	21 Oct. 2008 19:00:00
			Fisk	22 Oct. 2008 15:00:00
B_r	18 Apr. 2009 05:00:00	446	Parker	13 Apr. 2009 16:00:00
			Fisk	14 Apr. 2009 02:00:00
V_t	13 Oct. 2008 05:00:00	498	Parker	9 Oct. 2008 03:00:00
			Fisk	9 Oct. 2008 15:00:00
V_n	21 Mar. 2009 07:00:00	432	Parker	16 Mar. 2009 14:00:00
			Fisk	17 Mar. 2009 04:00:00

The remaining Fisk field results are shown on 17 November 1996 (day 7 of CR1916) and do not map to a PCH. On 29 November 1996 (day 19 of CR1916), the Fisk model either maps to a southern PCH or a northern PCH which extends into CR1917. The top panel of Figure 7 shows the change of B_r from negative to positive between the last two maxima and explains the change in mapping from the southern to the northern PCHs. The last two mapping results from the Fisk field are on 2 December 1996 (day 22 during CR1916) on 13 December 1996 (day 6 during CR1917), both of which are inside well-developed northern PCHs.

5.2. *2008/2009 solar minimum*

Figure 9 shows the Carrington maps for CRs 2074 - 2076 and 2080 - 2082 during the 2008/2009 solar minimum of which the details are summarised in Table 5. Five (V_r, B_t, B_r, V_t and V_n in Table 5) of the eight maxima from Table 2 are traced to the photosphere in Figure 9. The other maxima are not traced since their maxima occurs close to the already-traced maxima. Figure 9(a) shows three blue circles located on the SWSS equator which corresponds to the date of maximum power of the periodicity on 17 September 2008 (day 73 of Figure 5(a)), and the two 5% decreases from the maximum on

7 September 2008 and 29 September 2008 (days 63 and 85 in Figure 5(a)). Figure 9(b) shows two CRs with the locations of the field line tracing from the maxima and ±5% lines from Figures 5(b) and 5(f) representing the blue and yellow circles and crosses respectively. The solid red horizontal lines show the mapping range using the Fisk model for the maximum shown in Figure 5(b), while the dashed red horizontal lines (across the two Carrington maps) show the mapping for the maximum related to Figure 5(e). Figures 9(c) and 9(d) show the same as the previous figure, but now the blue symbols are related to Figure 5(e) (maximum located on 17 April 2009 (day 285)) and the yellow symbols are related to Figure 5(c) (maximum located on 21 March 2009 (day 258)).

Figure 9(a) shows that the PFSS model maps down to locations close to the solar equator, where the Fisk field maps exclusively to the north solar pole since B_r is negative at the first maximum shown on the middle panel of Figure 7. The Fisk model traces down into the northern PCHs between 3 September 2008 (day 5 during CR2074) and 24 August 2008 (day 26 during CR2074). There are two equatorial CHs visible between 2 and 6 September 2008 (days 4 to 8 during CR2074) located a few degrees below the equator extending to mid-latitudes, and 10 to 12 September 2008 (days 12 to 14 during the same CR) located a few degrees above the equator extending to mid-latitudes. The PFSS model maps down close to CH activity during these two instances, while no clear CH activity is observed at the location of the third and final mapping on 23 September 2008 (day 25 during CR2074).

Figure 9(b) also shows the PFSS model mapping down close to the solar equator. A well-established equatorial CH is observed between 24 and 28 October 2008 (days 2 and 6 during CR2076) which is a repetition of the CH observed in the previous CR between 29 September and 2 October 2008 (days 4 and 7 during CR2075), which was captured by the tracing process. The Fisk model maps to well-developed northern PCHs during CR2075 and 2076 due to the negative polarity of B_r (middle panel of Figure 7). The field line tracing results of the PFSS model in Figures 9(c) and 9(d) are further away from the solar equator than during previous CRs. The northern mid-latitude CHs visible on 16 March 2009 (day 8 during CR2081) as well as the small northern mid-latitude CH visible on 26 March 2009 (day 18 during the same CR) are well captured by the PFSS model. Mapping locations that are not close to CH activity include 30 March 2009 (day 22 during CR2081), 13 April 2009 (day 9 during CR2082), and 22 April 2009 (day 18 during CR2082). Furthermore, the mapping of the Fisk model captures the southern PCHs (due to the positive B_r polarity in the middle panel of Figure 7) during the last three CRs of Figure 9.

Table 6. 2019/2020 solar minimum temporal field line tracing details between L1 and the SWSS for the Fisk and Parker HMFs.

	L1	V_r (km/s)	Model	SWSS
V_r	22 Aug. 2019 05:00:00	345	Parker	16 Aug. 2019 10:00:00
			Fisk	17 Aug. 2019 02:00:00
B_r	6 Aug. 2019 14:00:00	502	Parker	2 Aug. 2019 13:00:00
			Fisk	3 Aug. 2019 00:00:00
B_t	20 Dec. 2019 04:00:00	430	Parker	15 Dec. 2019 11:00:00
			Fisk	16 Dec. 2019 00:00:00
B_n	10 Jan. 2020 20:00:00	339	Parker	4 Jan. 2020 21:00:00
			Fisk	5 Jan. 2020 14:00:00

5.3. *2019/2020 solar minimum*

Figure 10 shows the Carrington maps for CRs 2219 - 2221 and CRs 2224 - 2226 during the 2019/2020 solar minimum of which the details are summarised in Table 6. Four (V_r, B_r, B_t and B_n in Table 6) of the eleven maxima from Table 3 are traced to the photosphere in Figure 10. The other maxima are not traced since their maxima occurs close to the already-traced maxima. Figures 10(a) and 10(b) show the locations of the mapping related to the first maximum observed for B_r (day 66 of Figure 6(d)) and V_r (day 82 of Figure 6(a)). The second maximum power of periodicity for B_t (day 202 of Figure 6(e)) and B_n (day 223 of 6(f)) maps down to the photosphere during CRs 2224 - 2226 in Figures 10(c) and 10(d). Figure 10(b) (CR2220) shows two instances where the PFSS model maps near the solar equator and two instances where it maps near the solar poles. On 2 August 2019 (day 8 during CR2220) the PFSS model maps into a well-developed CH extending from mid-latitudes to the solar equator. Northern PCHs are visible during CRs 2220 and 2221 (Figure 10(b)) and are mapped by the Fisk HMF due to the positive polarity of the maxima shown in the first half of the bottom panel of Figure 7. Both the PFSS and Fisk models map to a PCH on 6 August 2019 (day 12 during CR2220). The re-

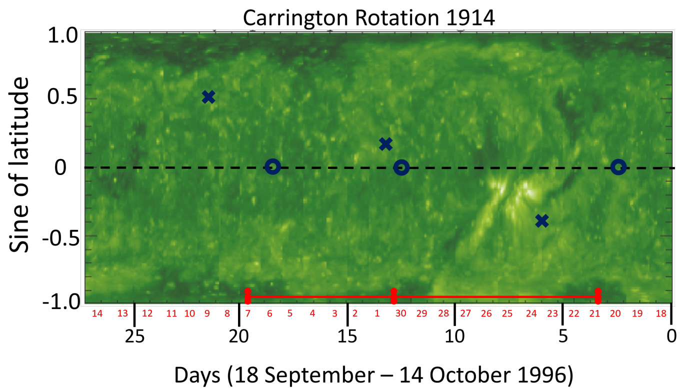

(a)

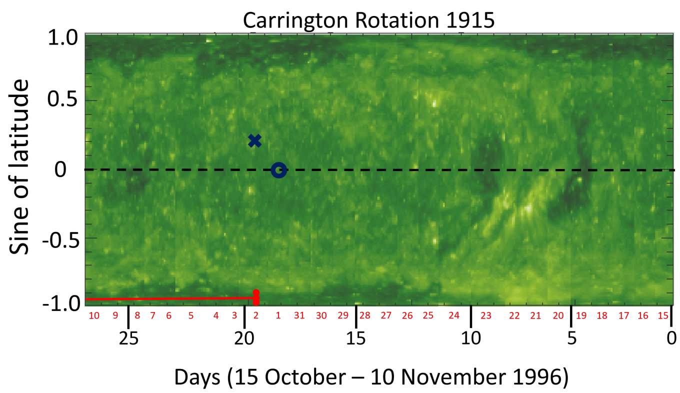

(b)

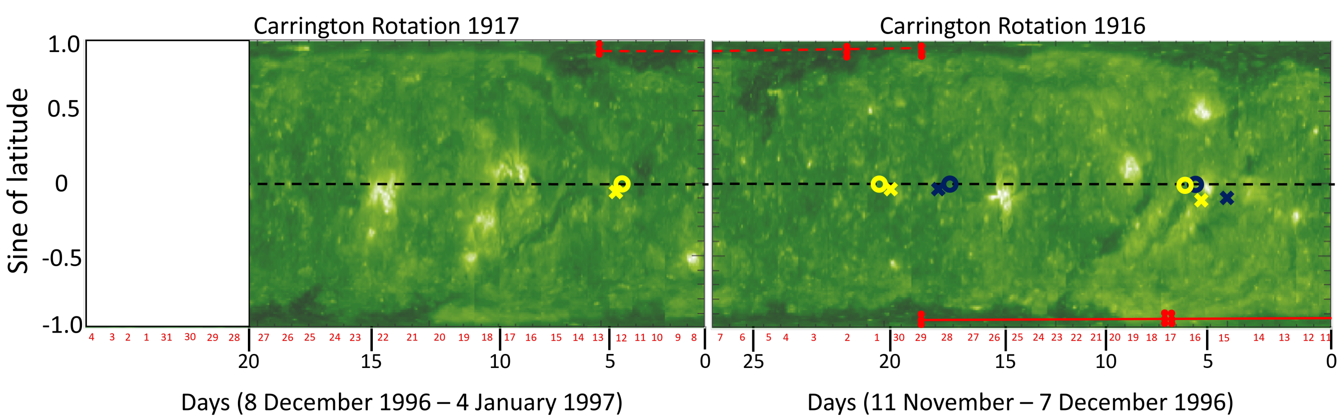

(c)

Figure 8. Carrington maps for Carrington rotations (a) 1914, (b) 1915, (c) 1916 and 1917. The horizontal axis runs chronologically from right to left (from the first day to the 27th day of each Carrington rotation). The calendar dates are shown in red for ease of reference. The vertical axis is the sine of the solar latitude from -1 to 1 with 0 at the solar equator (indicated with a black vertical dashed line). Blue and yellow symbols refer to the mapping of the PFSS model. The circles are the entry points at the source surface and the crosses are the landing points at the photosphere. The red symbols refer to the mapping of the Fisk HMF. The vertical lines show the uncertainty in heliographic latitude, while the horizontal solid and dashed lines group together the traces from peak power and their 5% reduction from Figure 4. The blank areas represent missing data, for example day 20 - 27 of CR1917.

maining northern PCH activity, extending into CR2221 (up until 31 August 2019 (day 10 during CR2221)) is captured by the Fisk field. On 16 August 2019 (day 22 during CR2220) the PFSS maps down to a southern PCH while on 30 August 2019 (day 9 during CR2221) it maps down to a location with little CH activity. It appears that the PFSS model does not map to the well-established equatorial-to-mid-latitude CH visible on 29 August 2019 (day 8 during CR2221), although the PFSS model did map to this CH during the previous CR on 2 August 2019. During CRs 2224 to 2226 (Figures 10(c) and 10(d)) the PFSS model tends to map towards the polar regions as is the case for the Fisk model. Well-established southern PCHs starting on 5 December 2019 (day 23 during CR2224) and extending to 14 January 2020 (day 9 during CR2226) are captured by the Fisk field results. The Fisk field maps to the southern PCHs observed during CRs 2224 and 2226 due to the negative polarity of B_r shown in the second half of the bottom panel of Figure 7. During this solar minimum epoch, it seems the PFSS model is more likely to map to the solar poles than to the solar equator, in contrast to what was observed during the previous solar minimum epoch.

6. DISCUSSION AND CONCLUSION

This study focused on the identification of periodic signals at the L1 position using the solar wind velocity and proton number density data from the WIND spacecraft, and the IMF data from the ACE spacecraft during the 1996/1997, 2008/2009, and 2019/2020 solar minima. We focused on periodicities between 26 and 28 days which is close to the solar synodic equatorial rotation rate. This is also the rotation rate of rigidly rotating CHs. To establish whether the periodic signals observed at L1 are related to the locations of CHs, the magnetic field lines are traced in the ecliptic plane from L1 to the SWSS assuming a Fisk field and for comparison also a Parker field. The tracing of field lines between the SWSS and the photosphere is done using the Fisk HMF model for the Fisk field lines and compared with the results of a PFSS model which arrives at the SWSS trough a Parker spiral. Table 7 summarises the details of whether a field line, either Fisk or Parker (PFSS), maps to a CH or not. The HMF models (column 1), the date at which each field line passed the SWSS (column 2), the field line trace from the −5% reduction to the left of the maximum (column 3), the field line trace at the maximum (column 4), and the field line trace from the −5% reduction to the right of the maximum (column 5) are shown in the header of Table 7. Y indicates the field line traced to a CH and N indicates the field line did not trace to a CH. The normalised O^{7+}/O^{6+} ratio is also used in the identification of the solar wind originating from CHs. Zhao et al. (2017) explain that a low heavy ion charge state ratio (O^{7+}/O^{6+}) is expected from CHs. The Appendix shows the analysis of these oxygen ratios for the 2008/2009 and 2019/2020 solar minima. Our results confirm the magnetic field lines traced in this study originate from PCHs and PCH boundaries as shown in the Carrington maps of Figures 9 and 10.

The solar minimum of 1996/1997 had a total of 9 mappings for both the PFSS and Fisk models respectively. Note the change in magnetic field polarity (from negative to positive) between the last two maxima shown in the top panel of Figure 7 (day 19 of CR1916 in Figure 8(c). The PFSS model did not map to CHs in any of the cases during this solar minimum, but did map to locations close to (within 10° in both latitude and longitude) CH activity in 2/9 ($\sim$ 22%) cases (day 6 of CR1914 and day 6 of CR1916). The Fisk model mapped down to locations of CH activity in 7/9 ($\sim$ 78%) cases.

Table 7. Details of magnetic field line tracing to CHs for the two HMF models. Y indicates a field line mapped into a CH, while N indicates a field lines mapped outside a CH.

Model	SWSS	−5% (L)	Max	−5% (R)
Fisk	30 Sept. 1996	Y	Y	Y
P & PFSS	30 Sept. 1996	Y	N	N
Fisk	17 Nov. 1996	Y	N	Y
P & PFSS	16 Nov. 1996	N	N	N
Fisk	29 Nov. 1996	N	Y	Y
P & PFSS	28 Nov. 1996	Y	N	N
Fisk	13 Sept. 2008	Y	Y	Y
P & PFSS	12 Sept. 2008	Y	N	N
Fisk	9 Oct. 2008	Y	Y	Y
P & PFSS	9 Oct. 2008	Y	N	N
Fisk	22 Oct. 2008	Y	N	Y
P & PFSS	21 Oct. 2008	N	Y	N
Fisk	17 Mar. 2009	Y	Y	N
P & PFSS	16 Mar. 2009	Y	Y	N
Fisk	14 Apr. 2009	Y	Y	Y
P & PFSS	13 Apr. 2009	N	N	N
Fisk	3 Aug. 2019	Y	Y	Y
P & PFSS	2 Aug. 2019	N	Y	N
Fisk	17 Aug. 2019	Y	Y	Y
P & PFSS	16 Aug. 2019	Y	Y	N
Fisk	16 Dec. 2019	Y	Y	Y
P & PFSS	15 Dec. 2019	N	Y	Y
Fisk	4 Jan. 2020	Y	Y	Y
P & PFSS	5 Jan. 2020	Y	N	Y

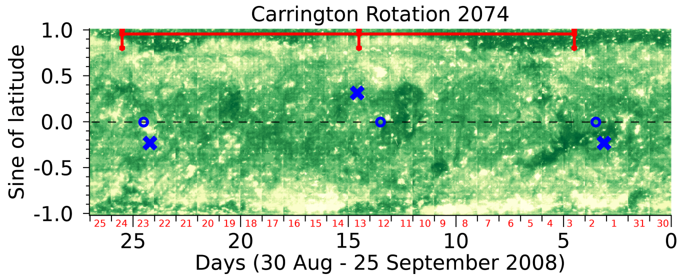

(a)

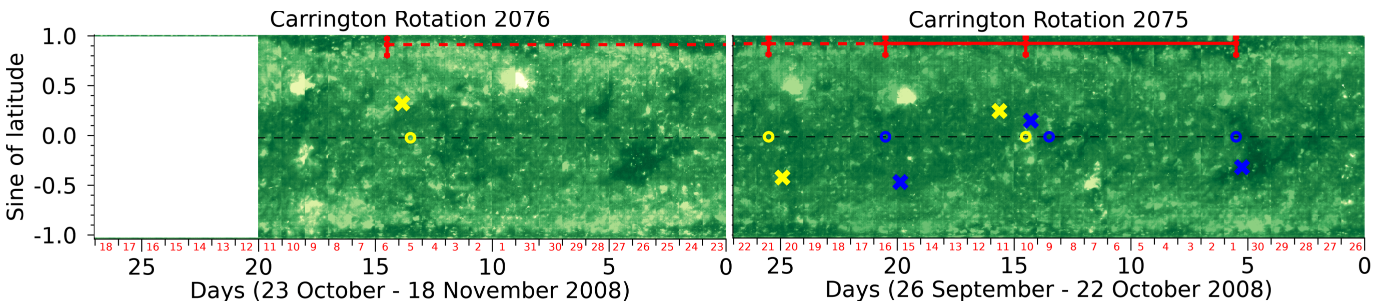

(b)

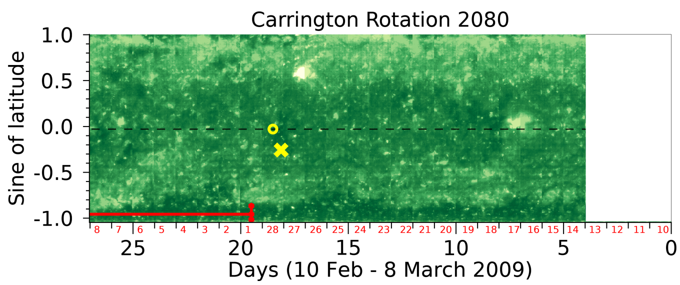

(c)

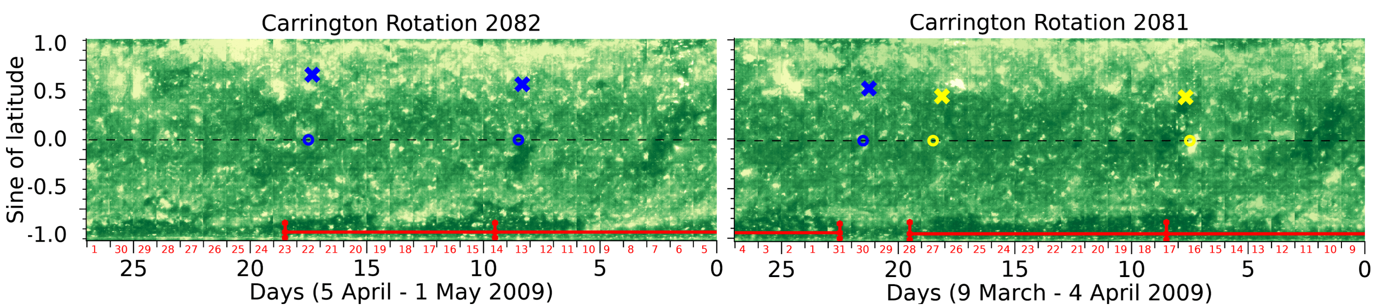

(d)

Figure 9. Carrington maps for Carrington rotations (a) 2074, (b) 2075 - 2076, (c) 2080, and (c) 2081 - 2082. See Figure 8 for a description of the axes and the meaning of the colour labels.

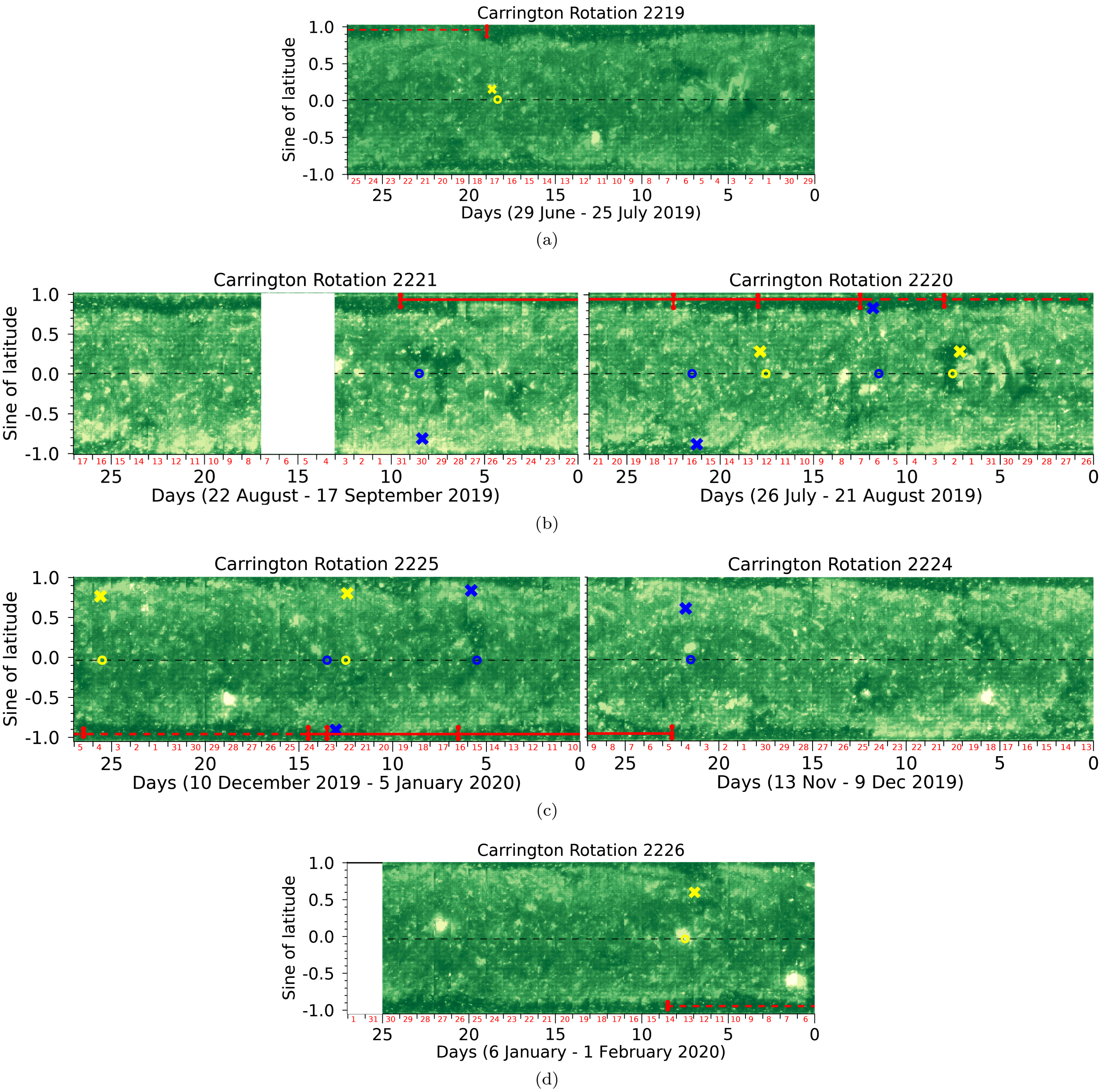

Figure 10. Carrington maps for Carrington rotations (a) 2219, (b) 2220 - 2221, (c) 2224 - 2225, and (d) 2226. See Figure 8 for a description of the axes and the meaning of the colour labels.

The two instances where the Fisk field did not map into a PCH are found on day 7 of CR1916, in contrast to the PFSS model which mapped close to a CH on this day. During this time a combination of equatorial, mid-latitude, and polar mappings were obtained from the PFSS model, although during CRs 1916 and 1917 (Figure 8(c)) the PFSS model maps exclusively to the equatorial region. This epoch had CHs missed by the PFSS model. These include the northern mid-latitude CH visible on 22 September 1996 (day 5 during CR1914 shown in Figure 8), a CH crossing the equator and visible on 19 October 1996 (day 5 during CR1915 shown in Figure 8(b)), and another CH crossing the equator during the same CR visible on 23 October 1996 (day 10 during CR1915).

During the 2008/2009 solar minimum, the PFSS model maps to equatorial to mid-latitude locations on the photosphere, while the Fisk model maps exclusively to the polar regions. During this solar minima, a total of 15 instances of each model were traced from their respective maxima at L1 to the photosphere. Comparing the photospheric mapping coordinates with the locations of CHs using both Carrington maps and solar synoptic maps, the PFSS model maps to the locations of CHs in 5/15 ($\sim$ 33%) cases and the Fisk traces to 13/15 ($\sim$ 87%) cases. The two instances where the Fisk model mapped outside the PCH are found on day 26 of CR2075 and day 20 of CR2081. Note that the former instance is an example where the Fisk field does not map to a PCH, but the PFSS model maps to a mid-latitude CH. Therefore, the periodicity observed on that day was dominated by a mid-latitude CH identified by the PFSS model. There are examples where CHs are visible, but neither of the models mapped to these locations. These examples include a northern PCH visible between 30 August to 1 September 2008 (days 1 to 3 during CR2074 shown in Figure 9(a)), a CH bordering the solar equator from the south between 25 to 27 October 2008 (days 3 to 5 during CR2076 shown in the left panel of Figure 9(b)), a southern PCH visible between 14 and 28 February 2009 (days 5 to 19 during CR2080 shown in Figure 9(c)), and a CH crossing the equator between 10 and 11 March 2009 (days 2 to 3 during CR2081 shown in the right panel of Figure 9(d)).

During the 2019/2020 solar minimum epoch, a total of 12 mapping results were obtained from both the PFSS and Fisk models respectively. The PFSS model mapped to CH locations in 5/12 cases ($\sim$ 42%) and the Fisk model mapped down to 12/12 (100%) cases. Note that the results from the PFSS model deviates from the previous solar minimum in the observation that it maps much closer to the polar regions. This could be attributed to using more accurate magnetograms in the PFSS model during the 2019/2020 solar minimum as mentioned in Section 2.3. A long lasting northern PCH between 1 and 17 September 2019 (days 11 to 27 during CR2221 shown in the left panel of Figure 10(b)) was not mapped by either model.

Considering the results from the three solar minima, it seems that a PFSS model is successful in connecting magnetic field lines to periodicities observed at L1 to CH locations in less than half of the investigated cases.

The Fisk model successfully connected magnetic field lines to the periodicities observed at L1 to CH locations in more than 78% of the cases during all three solar minima investigated. It is important to note the main difference between the models. Magnetograms are used as input for the PFSS model which ensures its results are based on the magnetic configuration of the photosphere. From the results, it seems that when a magnetic field is traced from the SWSS equator, the PFSS model maps close to the solar equator and mid-latitudes in most instances. In contrast, the dominant input parameter of the Fisk model is the tilt angle α. Field lines starting at the equator on the SWSS map exclusively to the solar poles.

The most important qualitative point in this study is the relationship shown between the theory of Fisk-type fields and spacecraft observations at L1. In most cases investigated, the Fisk model traces field lines to inside PCHs. This emphasises the influence of PCHs on plasma measurements in the ecliptic. Furthermore, there are examples where very little to no PCH activity is observed, and the Fisk field does not trace to these polar regions due to the orientation of the HCS (Figure 7). These examples include: CR1917 between 14 and 19 December 1996, the northern pole during CR2080 between 14 and 27 February 2009, CR2081 between 29 and 30 March 2009, CR2081 between 24 and 28 April 2009, the southern pole during CR2221 between 1 and 13 September 2019 and lastly, CR2224 between 21 and 24 November 2019.

There are examples where the Fisk model traces field lines to PCHs on a specific date, but in contrast, the PFSS tracing on that same date does not map to existing CHs. One example include 13 September 2008 during CR2074 (Figure 9(a)) where the northern PCH is mapped by the Fisk model, but the PFSS model maps to $\sim 30^{\circ}$ east (left) of a well-established CH. Another example include 13 and 22 April 2009 during CR2082 (left panel of Figure 9(d)) where the Fisk model maps to the southern PCH, and the PFSS model maps to the northern mid-latitudes with no CH activity. Similar examples are found during both the 1996/1997 and 2019/2020 solar minima. There are also two instances where the Fisk model did not map to a PCH, but the PFSS model mapped to a CH on that date. This asserts our notion that the Fisk and PFSS models are complimentary and should be viewed together when investigating solar wind disturbances at L1.

Since the Fisk model cannot, by design, map to the equatorial and mid-latitude regions, it will not map to CHs in these regions. The Fisk model maps exclusively to PCHs, while the PFSS model is more successful in mapping to CHs in the equatorial region. This study emphasises the importance of combining results from the PFSS and the Fisk models to provide a more complete description of the connectivity between solar wind and magnetic field disturbances observed at L1 with their CH origin. Lastly, this study illustrates the large influence of PCHs on solar wind and magnetic field components within 1 AU of the sun.

We thank the anonymous reviewer for their insightful and helpful comments that have improved this manuscript. We thank Micah J. Weberg for his advice in obtaining WIND and ACE data. All authors acknowledge UK Science and Technology Facilities Council (STFC) for IDL support. PJS thanks the National Research Foundation of South Africa (Ref Numbers TTK2204183656) for research support. Opinions expressed and conclusions arrived at are those of the authors and are not necessarily to be attributed to the NRF. The responsibility of the contents of this work is with the authors. GJJB and SR acknowledge the UK Science and Technology Facilities Council (STFC) for support from grant no. ST/X001008/1. The data that support the findings of this study are available from the corresponding author upon reasonable request.

Facilities: ACE, WIND, SOHO, SDO, NOAA

Software: Python (Hunter 2007; Caswell et al. 2023), Additional data analyses were done using IDL version 9.0 (Exelis Visual Information Solutions, Boulder, Colorado).

REFERENCES

Altschuler, M. D., & Newkirk, G. 1969, SoPh, 9, 131, doi: 10.1007/BF00145734

Balogh, A., & Erdõs, G. 2013, SSRv, 176, 177, doi: 10.1007/s11214-011-9835-3

Benevolenskaya, E. 2001, EIT Synoptic Maps. http://sun.stanford.edu/synop/EIT/

Benevolenskaya, E. E., Kosovichev, A. G., & Scherrer, P. H. 2001, ApJL, 554, L107, doi: 10.1086/320925

Carrasco, V. M. S., & Vaquero, J. M. 2021, Research Notes of the American Astronomical Society, 5, 181, doi: 10.3847/2515-5172/ac19a2

Caswell, T. A., Sales De Andrade, E., Lee, A., et al. 2023, matplotlib/matplotlib: REL: v3.7.2, v3.7.2, Zenodo, Zenodo, doi: 10.5281/zenodo.8118151

Contopoulos, I. 2013, SoPh, 282, 419, doi: 10.1007/s11207-012-0154-y

Domingo, V., Fleck, B., & Poland, A. I. 1995, SoPh, 162, 1, doi: 10.1007/BF00733425

ESA. 2023, Soho Science Archive. https://ssa.esac.esa.int/ssa/#/pages/search

Fisk, L. A. 1996, J. Geophys. Res., 101, 15547, doi: 10.1029/96JA01005

Fisk, L. A., Zurbuchen, T. H., & Schwadron, N. A. 1999, ApJ, 521, 868, doi: 10.1086/307556

Freeland, S. L., & Handy, B. N. 1998, SoPh, 182, 497, doi: 10.1023/A:1005038224881

Garraffo, C., Cohen, O., Drake, J. J., & Downs, C. 2013, ApJ, 764, 32, doi: 10.1088/0004-637X/764/1/32

Gilbert, J. A., Zurbuchen, T. H., & Fisk, L. A. 2007, ApJ, 663, 583, doi: 10.1086/518099

Gloeckler, G., Cain, J., Ipavich, F. M., et al. 1998, SSRv, 86, 497, doi: 10.1023/A:1005036131689

Hamada, A., Asikainen, T., Virtanen, I., & Mursula, K. 2018, SoPh, 293, 71, doi: 10.1007/s11207-018-1289-2

Hoeksema, J. T. 1984, PhD thesis, Stanford University, California

—. 1995, SSRv, 72, 137, doi: 10.1007/BF00768770

Hofmeister, S. J., Utz, D., Heinemann, S. G., Veronig, A., & Temmer, M. 2019, A&A, 629, A22, doi: 10.1051/0004-6361/201935918

Hunter, J. D. 2007, Computing in Science and Engineering, 9, 90, doi: 10.1109/MCSE.2007.55

Jain, R. N., Choudhary, R. K., & Imamura, T. 2024, MNRAS, 529, L123, doi: 10.1093/mnrasl/slae008

Jian, L. K., Russell, C. T., & Luhmann, J. G. 2011, SoPh, 274, 321, doi: 10.1007/s11207-011-9737-2

Lepping, R. P., Acũna, M. H., Burlaga, L. F., et al. 1995, SSRv, 71, 207, doi: 10.1007/BF00751330

Li, B., Cairns, I. H., Gosling, J. T., et al. 2016, Journal of Geophysical Research (Space Physics), 121, 925, doi: 10.1002/2015JA021853

Luhmann, J. G., Li, Y., Lee, C. O., et al. 2022, Space Weather, 20, e2022SW003110, doi: 10.1029/2022SW003110

Mursula, K., & Zieger, B. 1996, J. Geophys. Res., 101, 27077, doi: 10.1029/96JA02470

Neugebauer, M., & Snyder, C. W. 1962, Science, 138, 1095, doi: 10.1126/science.138.3545.1095.a

NOAA. 1996-2020, Solar Synoptic Analysis. https://www.ngdc.noaa.gov/stp/space-weather/solar-data/solar-imagery/composites/full-sun-drawings/boulder/

Ogilvie, K. W., Chornay, D. J., Fritzenreiter, R. J., et al. 1995, SSRv, 71, 55, doi: 10.1007/BF00751326

Owens, M. J., & Forsyth, R. J. 2013, Living Reviews in Solar Physics, 10, 5, doi: 10.12942/lrsp-2013-5

Parenti, S., Chifu, I., Del Zanna, G., et al. 2021, SSRv, 217, 78, doi: 10.1007/s11214-021-00856-1

Parker, E. N. 1958, ApJ, 128, 664, doi: 10.1086/146579

Pesnell, W. D., Thompson, B. J., & Chamberlin, P. C. 2012, SoPh, 275, 3, doi: 10.1007/s11207-011-9841-3

Posner, A., Zurbuchen, T. H., Schwadron, N. A., et al. 2001, J. Geophys. Res., 106, 15869, doi: 10.1029/2000JA000112

Prabhakaran Nayar, S. R., Radhika, V. N., Revathy, K., & Ramadas, V. 2002, SoPh, 208, 359, doi: 10.1023/A:1020565831926

Richardson, I. G., & Cane, H. V. 2010, SoPh, 264, 189, doi: 10.1007/s11207-010-9568-6

Riley, P., Caplan, R. M., Downs, C., Linker, J. A., & Lionello, R. 2022, Journal of Geophysical Research (Space Physics), 127, e30261, doi: 10.1029/2022JA030261

Schatten, K. H., Wilcox, J. M., & Ness, N. F. 1969, SoPh, 6, 442, doi: 10.1007/BF00146478

Scherrer, P. H., Bogart, R. S., Bush, R. I., et al. 1995, SoPh, 162, 129, doi: 10.1007/BF00733429

Scherrer, P. H., Schou, J., Bush, R. I., et al. 2012, SoPh, 275, 207, doi: 10.1007/s11207-011-9834-2

Schrijver, C. J., & De Rosa, M. L. 2003, SoPh, 212, 165, doi: 10.1023/A:1022908504100

SILSO World Data Center. 1996-2020, International Sunspot Number Monthly Bulletin and online catalogue

Simpson, J. A., Anglin, J. D., Bothmer, V., et al. 1995, Science, 268, 1019, doi: 10.1126/science.268.5213.1019

Singh, Y. P., & Badruddin. 2019, SoPh, 294, 27, doi: 10.1007/s11207-019-1413-y

Smith, C. W., L'Heureux, J., Ness, N. F., et al. 1998, SSRv, 86, 613, doi: 10.1023/A:1005092216668

Stakhiv, M., Landi, E., Lepri, S. T., Oran, R., & Zurbuchen, T. H. 2015, ApJ, 801, 100, doi: 10.1088/0004-637X/801/2/100

Stansby, D., Horbury, T. S., & Matteini, L. 2019, MNRAS, 482, 1706, doi: 10.1093/mnras/sty2814

Steyn, P. J., & Burger, R. A. 2020, ApJ, 902, 33, doi: 10.3847/1538-4357/abb2a5

Strauss, R. D. T., Dresing, N., & Engelbrecht, N. E. 2017, ApJ, 837, 43, doi: 10.3847/1538-4357/aa5df5

Thompson, B. J., Newmark, J. S., Gurman, J. B., et al. 1997, in ESA Special Publication, Vol. 404, Fifth SOHO Workshop: The Corona and Solar Wind Near Minimum Activity, ed. A. Wilson, 779

Thompson, W. T. 2006, A&A, 449, 791, doi: 10.1051/0004-6361:20054262

Tsichla, M., Gerontidou, M., & Mavromichalaki, H. 2019, SoPh, 294, 15, doi: 10.1007/s11207-019-1403-0

Wang, Y.-M., Hawley, S. H., & Sheeley, Neil R., J. 1996, Science, 271, 464, doi: 10.1126/science.271.5248.464

Wang, Y. M., Ko, Y. K., & Grappin, R. 2009, ApJ, 691, 760, doi: 10.1088/0004-637X/691/1/760

Wang, Y. M., & Sheeley, N. R., J. 1992, ApJ, 392, 310, doi: 10.1086/171430

Wilson, Lynn B., I., Brosius, A. L., Gopalswamy, N., et al. 2021, Reviews of Geophysics, 59, e2020RG000714, doi: 10.1029/2020RG000714

Yang, L. P., Feng, X. S., Xiang, C. Q., et al. 2012, Journal of Geophysical Research (Space Physics), 117, A08110, doi: 10.1029/2011JA017494

Yeates, A. R., Amari, T., Contopoulos, I., et al. 2018, SSRv, 214, 99, doi: 10.1007/s11214-018-0534-1

Zhao, L., Landi, E., Lepri, S. T., et al. 2017, ApJ, 846, 135, doi: 10.3847/1538-4357/aa850c

Zurbuchen, T. H., Schwadron, N. A., & Fisk, L. A. 1997, J. Geophys. Res., 102, 24175, doi: 10.1029/97JA02194

APPENDIX

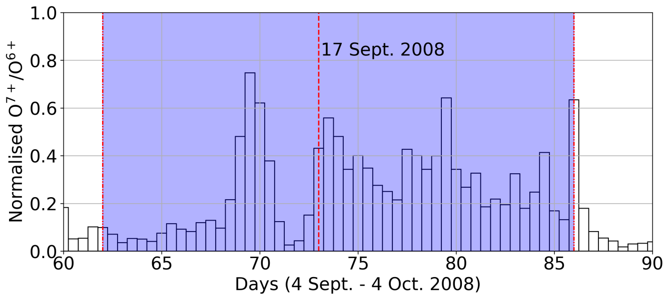

(a)

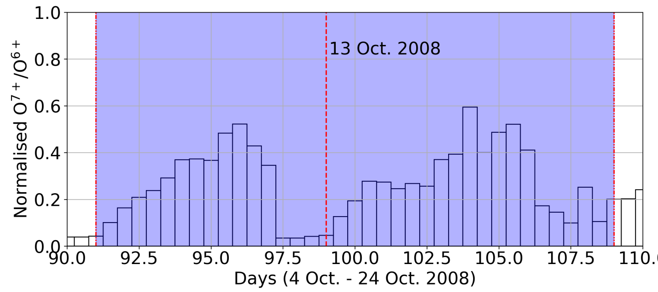

(b)

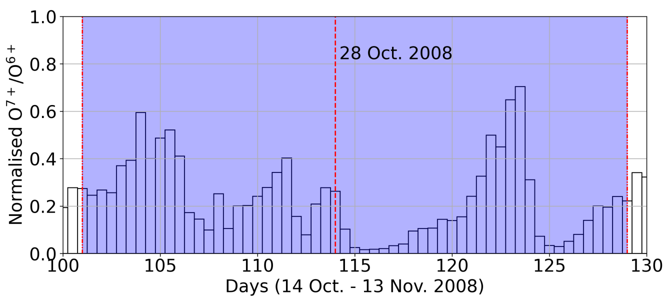

(c)

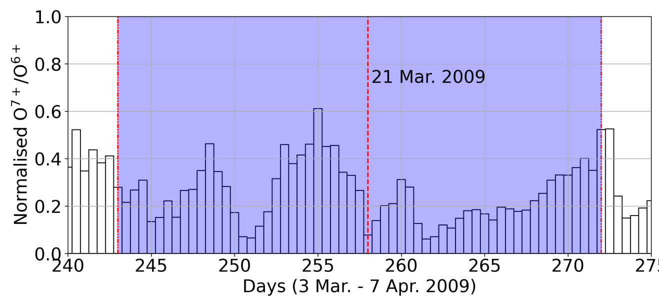

(d)

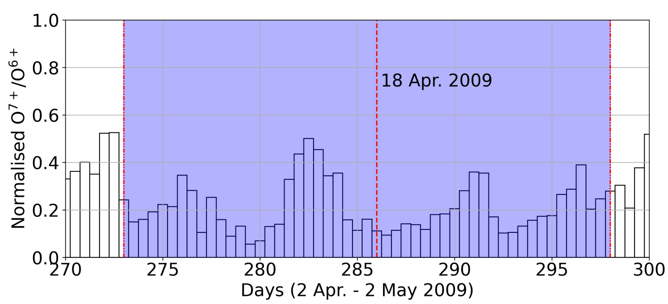

(e)

Figure 11. Normalised O^{7+}/O^{6+} ratios for the 2008-2009 solar minimum. The bottom axis of each panel indicates the number of days since 6 July 2008. The red dashed vertical line (in the middle of the blue shaded area) shows the date of the maximum signal according to the wavelet analysis of Section 4.2 while the left and right edges of the blue area indicate the 5% decrease from the maximum signal (see Figure 5). The corresponding Carrington Rotation of each panel, according to Section 5.2 and Figure 9, is (a) CR2074, (b) CR2075, (c) CR2075 - 2076, (d) CR2080 - 2081 and (e) CR2081 - 2082

Zhao et al. (2017) investigated the proton speed and heavy ion charge state ratios (O^{7+}/O^{6+}) of different coronal source solar wind types between 1998 to 2011, including 2000 to 2002 (solar maximum) and 2007 to 2009 (solar minimum.) Their results show that proton speed alone is not sufficient to identify PCHs since solar wind speeds from PCHs range between 300 $\mathrm{kms^{-1}}$ and 800 $\mathrm{kms^{-1}}$. Furthermore, Zhao et al. (2017) show by correlating EIT Carrington maps with the oxygen ratio using PFSS that the O^{7+}/O^{6+} ratio of the solar wind types is ordered such that the helmet-streamer and active region winds have the highest ratio (normalised over the dataset) while CH-boundary and CH winds have the lowest ratios.

The two-hour averaged O^{7+}/O^{6+} ratios (normalised in terms of the maximum value observed during one year) measured by ACE/SWICS (Gloeckler et al. 1998) during the 2008-2009 and 2019-2020 solar minima are presented in

Figures 11 and 12. The maximum O^{7+}/O^{6+} ratio during the 2008-2009 and 2019-2020 solar minima is 0.27 and 0.41, respectively. Since the two maxima are not the same, the results from the two solar minima are not directly compared with each other. Each panel in Figures 11 and 12 is linked to its corresponding Carrington Rotation from Sections 5.2 and 5.3.

A low O^{7+}/O^{6+} ratio is observed at the start of the blue shaded region in Figure 11(a) which corresponds to Days 5 to 10 in Figure 9(a) where a PCH is observed. Next, the PCH boundary is reached and the O^{7+}/O^{6+} ratio increases (Day 69 in Figure 11(a)) after which it decreases (Day 72), increases again (Day 74), and continues on a relative high level up until the 5% decrease from the maximum value is reached. The low O^{7+}/O^{6+} ratios approximately correspond to visible PCHs in Figure 9(a). Although Figure 11(b) shows a drop in O^{7+}/O^{6+} ratio on Day 98, only a comparatively small PCH (dark green pixels) is observed during CR2075 in Figure 9(b). There is a larger PCH earlier during this CR on Day 10 of CR2075 which remains within the window of the 5% decrease from the maximum signal observed. Figure 11(c) shows an increasing and decreasing trend which corresponds to the scattered PCHs and PCH boundaries shown in Figure 9(b) during CR2076. A similar increase and decrease of O^{7+}/O^{6+} ratios are observed in Figures 11(d) and 11(e) corresponding to the PCH boundaries and PCHs from Figures 9(c) and 9(d). The assumption of a constant solar wind speed between L1 and the photosphere (see Section 3) is idealistic (also see comments made by Zhao et al. (2017)) and therefore the exact dates at which the maximum signal is observed in the wavelet analyses will not necessarily correspond to the exact dates where the O^{7+}/O^{6+} ratio is a minimum. However, the results show that the minima in the O^{7+}/O^{6+} ratios occur in the vicinity of the date of the maximum observed signal.

CR2219 and 2220 show long lasting, continuous PCHs in Figures 10(a) and 10(b) which corresponds to the relative low O^{7+}/O^{6+} ratios in Figure 12(a). This trend continues into CR2221 which corresponds to the Figure 12(b). The PCH in the southern hemisphere during CR2224 and 2225 vary in size and intensity (Figure 10(c)) which corresponds to the increasing and decreasing O^{7+}/O^{6+} ratios shown in Figure 12(c). Note there is a data gap in the latter part of Figure 12(c) and at the start of Figure 12(d). A large, continuous PCH during the latter part of CR2225 and at the start of CR2226 corresponds well with the low O^{7+}/O^{6+} ratios observed in Figure 12(d).

Combining the results from the wavelet analyses (Sections 4.2 and 4.3), the Carrington maps (Sections 5.2 and 5.3) and the results from the O^{7+}/O^{6+} ratios, provide a comprehensive description about whether the investigated solar wind originates from a PCH or not.

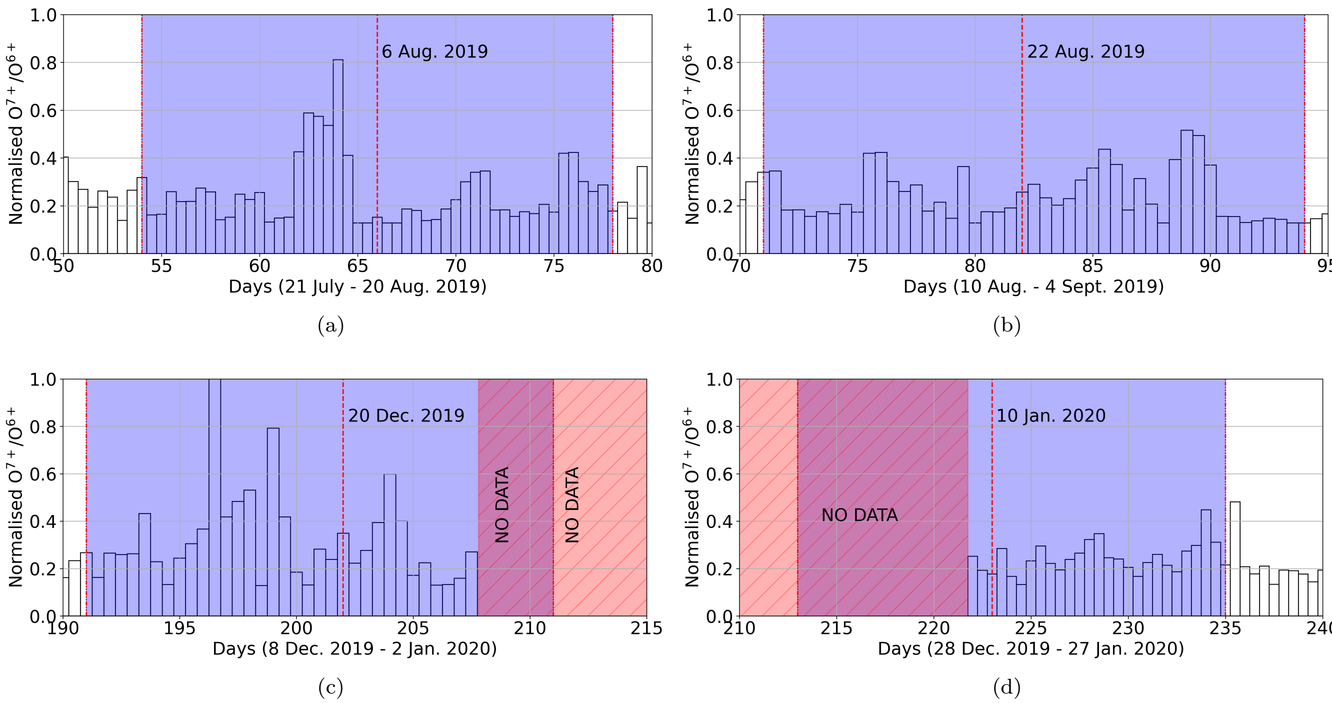

Figure 12. Normalised O^{7+}/O^{6+} ratios for the 2019-2020 solar minimum. The bottom axis of each panel indicates the number of days since 1 June 2019. The red dashed vertical line (in the middle of the blue shaded area) shows the date of the maximum signal according to the wavelet analysis of Section 4.3 while the left and right edges of the blue area indicate the 5% decrease from the maximum signal (see Figure 6). The corresponding Carrington Rotation of each panel, according to Section 5.3 and Figure 10, is (a) CR2219 - 2220, (b) CR2220 - 2221, (c) CR2224 - 2225, and (d) CR2225 - 2226.